Acta Materialia 255 (2023) 118986

Contents lists available at ScienceDirect

Acta Materialia

journal homepage: www.elsevier.com/locate/actamat

Full length article

Strong impact of spin fluctuations on the antiphase boundaries of weak itinerant ferromagnetic Ni_3Al

Xiang Xu [a,b], Xi Zhang [b,*], Andrei Ruban [c,d], Siegfried Schmauder [a], Blazej Grabowski [b]

[a] Institute for Materials Testing, Materials Science and Strength of Materials, University of Stuttgart, Pfaffenwaldring 32, 70569 Stuttgart, Germany
[b] Institute for Materials Science, University of Stuttgart, Pfaffenwaldring 55, 70569 Stuttgart, Germany
[c] KTH Royal Institute of Technology, SE-100 44, Stockholm, Sweden
[d] Materials Center Leoben Forschung GmbH, A-8700 Leoben, Austria

ARTICLE INFO

Keywords:
Antiphase boundary
Ab initio calculations
Nickel-aluminide
Computational thermodynamics
Paramagnetism

ABSTRACT

Antiphase boundaries (APBs) are crucial to understand the anomalous temperature dependence of the yield stress of Ni_3Al. However, the required, accurate prediction of temperature-dependent APB energies has been missing. In particular, the impact of magnetism at elevated temperatures has been mostly neglected, based on the argument that Ni_3Al is a weak ferromagnet. Here, we show that this is an inappropriate assumption and that – in addition to anharmonic and electronic excitations – thermally-induced magnetic spin fluctuations strongly affect the APB energies, especially for the (100)APB with an increase of nearly up to 40% over the nonmagnetic data. We utilize an *ab initio* framework that incorporates explicit lattice vibrations, electronic excitations, and the impact of magnetic excitations up to the melting temperature. Our results prompt to take full account of thermally-induced spin fluctuations even for weak itinerant ferromagnetic materials. Consequences for large-scale modeling in Ni-based superalloys, e.g., of dislocations or the elastic–plastic behavior, can be expected.

1. Introduction

Ni-based superalloys are exceptional materials withstanding high pressures and temperatures in harsh environments, e.g., in turbine disc applications [1]. The strengthening mechanisms in these alloys rely mainly on ordered intermetallic phases, coherently embedded in the fcc Ni host matrix [2,3]. The typically utilized $L1_2$-ordered Ni_3Al intermetallic phase provides, among other beneficial features, a very unique strengthening mechanism on account of its specific yield stress behavior – the so-called yield stress anomaly (YSA). In particular, the yield stress of Ni_3Al increases strongly (more than a factor of five) with temperature from 77 K up to 1100 K [4,5]. The origin of YSA lies in an increasing amount of Kear-Wilsdorf locks, i.e., locks formed due to cross-slip of screw superpartial dislocations from an easy-glide {111} plane to a less favorable {100} plane [6], with temperature [5,7,8]. Between the dissociated superpartials, two planar defects are formed depending on the slip plane. These defects are the (100) and (111) antiphase boundaries (APBs; see Fig. 1), and they are believed to play a crucial role during the cross-slip and thus in explaining YSA [9–11].

Despite the great importance of the APBs, a comprehensive understanding of their formation Gibbs energies has been absent until now. Starting in the 1980s, many experimental works determined APB energies for Ni_3Al by measuring the extent of dislocation dissociation with transmission electron microscopy [5,7,8,12–16]. The respective data show typical uncertainties of ±8 to ±12% [15] and also appreciable scatter between different data sets. The scatter originates partly from off-stoichiometric Ni_3Al samples and varying types of impurity elements in different experiments [15]. Moreover, unavoidable defect-defect interactions suppress the dislocation dissociation and thereby substantially affect the measured dissociation distance [7,14,15,17], especially for (100)APBs after cross-slip. The determination of perfectly equilibrated APB energies is, thus, a highly non-trivial task.

Predictions of APB energies from *ab initio* calculations are a viable complementary approach, but they have been mostly limited to 0 K [18–20] or low temperature approximations [21]. In particular, the impact of magnetism on the APB energy in Ni_3Al at elevated temperatures has remained elusive. For Fe-based materials with strong magnetic moments such as Fe_3O_4 films it is known that APBs significantly affect the local magnetic state [22]. However, $L1_2$-Ni_3Al is a weak itinerant ferromagnetic material with a low Curie temperature $T_C \approx 41.5$ K [23] and one may expect that there is little impact of APBs on magnetism and vice versa. Thus, the paramagnetic behavior of Ni_3Al above ambient temperature and the respective entropy contribution to

* Corresponding author.
E-mail address: xi.zhang@imw.uni-stuttgart.de (X. Zhang).

https://doi.org/10.1016/j.actamat.2023.118986
Received 8 December 2022; Received in revised form 27 April 2023; Accepted 4 May 2023
Available online 11 May 2023

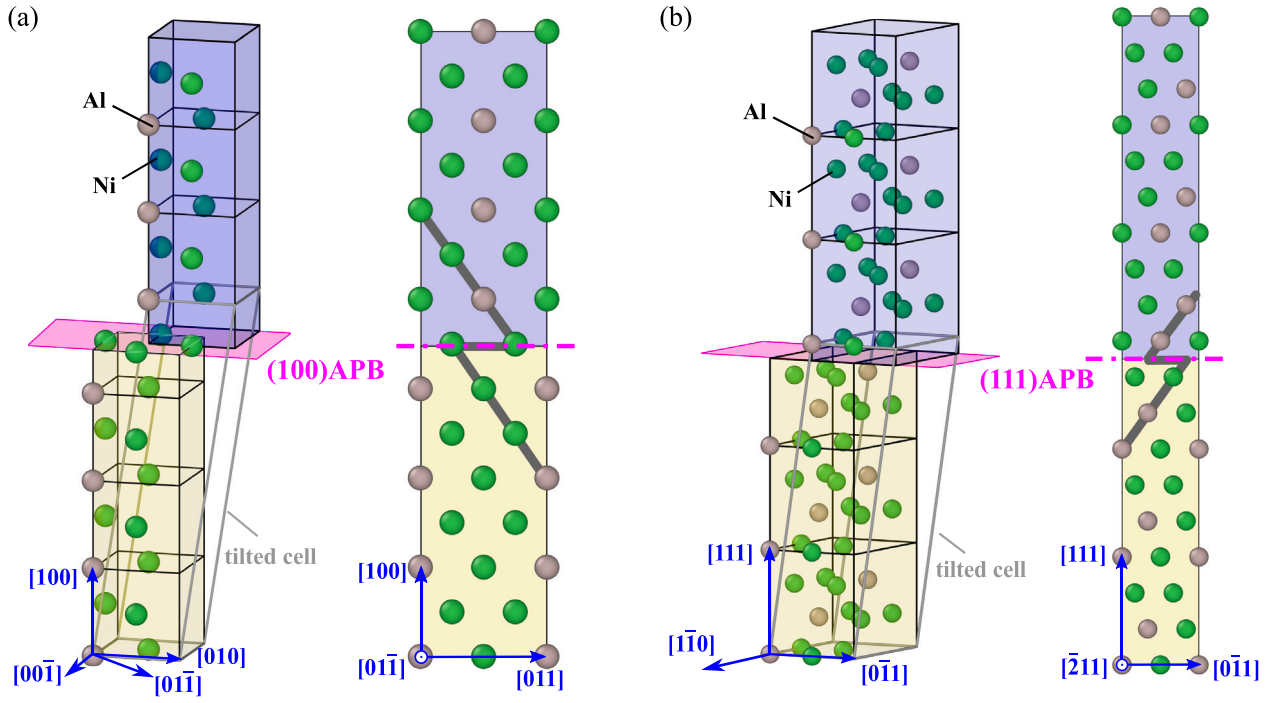

Fig. 1. Schematic models for the (100)APB and (111)APB. Each unit cube represents a unit cell which contains 4 atoms for the (100)APB and 12 atoms for the (111)APB, respectively. The labeled tilted cells in (a) and (b) represent a 1 × 1 × 4 supercell (with 16 atoms) for the (100)APB and a 1 × 1 × 3 supercell (with 36 atoms) for the (111)APB, respectively. The APB is highlighted by the magenta plane. In consistency with these models and with literature, we use the notation (100)APB and (111)APB in the text. The results apply however to all symmetrically equivalent planes. (For interpretation of the references to color in this figure legend, the reader is referred to the web version of this article.)

the APB energies have been rarely investigated, assuming that thermal magnetic excitations should give practically negligible contribution to the bonding and thermodynamic properties. Here, we demonstrate that thermal magnetic excitations do play a major role in predicting accurate APB energies in Ni_3Al at elevated temperatures.

In principle, thermal magnetic excitations, including the important impact of longitudinal spin fluctuations (LSFs) [24], can be accurately accounted for by using advanced *ab initio* approaches such as, for example the dynamical mean-field theory [25]. However, the application of such methods to large supercells to model APBs is not yet feasible. An alternative strategy is to utilize density functional theory (DFT) and to map DFT energies of specific constrained magnetic configurations to a magnetic Hamiltonian, which can be used for finite temperature modeling. This makes sense above the magnetic phase transition temperature, i.e., in the paramagnetic state [26]. At temperatures much higher than the corresponding magnetic phase transition, when magnetic short-range order effects can be neglected, this approach can be simplified further by using the single-site mean-field approximation for the magnetic contribution [27]. A conceptually and computationally demanding task remains the simultaneous account of thermal magnetic and other excitations such as vibrations [28].

The contribution from thermal atomic vibrations, including its anharmonic part, constitutes by itself a significant challenge, if an accurate description at elevated temperatures is required. Low temperature approximations such as, for example, the quasiharmonic approximation, impose inappropriate constraints at elevated temperatures [29] and therefore do not properly capture defect energies [29,30]. Application of renormalized, effective harmonic Hamiltonians cannot remedy the discrepancy because of the harmonic restriction. In contrast, approaches that are fundamentally based on the concept of thermodynamic integration can account for explicit thermal vibrations. In this respect, different developments have been put forward recently to speed up such calculations in combination with advanced sampling techniques [31,32].

In the present work, we propose a combination of state-of-the-art methods to simultaneously account for thermal magnetic excitations and explicit thermal atomic vibrations as well as the corresponding electronic excitations to predict accurate temperature dependent (100) and (111)APB energies of Ni_3Al up to the experimental melting point, T_m = 1668 K [33]. Specifically, we employ the single-site mean-field approximation for the spin fluctuation contribution utilizing DFT-based disordered local moment (DLM) calculations to capture both the transverse and longitudinal spin fluctuations [27]. To account for explicit thermal vibrations and electronic excitations on the *ab initio* level, we employ the recently developed direct upsampling methodology based on machine learning potentials [32].

2. Theory and computational details

2.1. General approach

The pressure P and temperature T dependent Gibbs energy required to form an APB (i.e., the APB energy) is obtained via

$$\gamma(P,T) = \frac{G_{\mathrm{APB}}(P,T) - G_{\mathrm{bulk}}(P,T)}{A_{\mathrm{APB}}(P,T)}, \tag{1}$$

where $G_{\mathrm{APB}}(P,T)$ and $G_{\mathrm{bulk}}(P,T)$ are the Gibbs energies of a supercell containing the APB and of the perfect bulk, respectively. Further, $A_{\mathrm{APB}}(P,T)$ represents the pressure and temperature-dependent area of the APB, which for the smallest unit area is related to the lattice constant a as

$$A_{\mathrm{APB}} = \begin{cases} a^2 & \text{for (100)APB,} \\ a^2 \cdot 3^{1/2} & \text{for (111)APB.} \end{cases} \tag{2}$$

As it is more convenient in the *ab initio* framework to control the volume rather than the pressure, we calculate first the Helmholtz energy $F(V,T)$ for the APB and the perfect bulk and then obtain the respective Gibbs energy by a Legendre transformation, i.e., $G(P,T)$ =

$F(V,T)+PV$. We focus in this work specifically on zero pressure which simplifies the Legendre transformation.

To account for the various relevant temperature-dependent thermal excitations, the Helmholtz energy is adiabatically decomposed as [31]

$$F(V,T) = E_{0K}(V) + F^{qh}(V,T) + F^{ah}(V,T) + F^{el}(V,T) + F^{mag}(V,T), \quad (3)$$

where E_{0K} denotes the 0 K total energy, $F^{qh}(V,T)$ and $F^{ah}(V,T)$ the contribution from non-interacting phonons (quasiharmonicity) and from *explicit* phonon–phonon interactions (anharmonicity), respectively. Further, F^{el} refers to the electronic free energy with the impact of thermal vibrations taken into account. The last term F^{mag} represents the magnetic free energy including spin fluctuations and the coupling to electronic excitations and thermal vibrations. The APB energy is decomposed in a similar manner as the Helmholtz energy into a sum of the different excitation contributions

$$\gamma(T) = \gamma_{0K} + \gamma^{qh}(T) + \gamma^{ah}(T) + \gamma^{el}(T) + \gamma^{mag}(T), \quad (4)$$

with the pressure dependence omitted for brevity.

All the free energy contributions were calculated at the *ab initio* level of accuracy. Specifically, the periodic Kohn–Sham DFT within the generalized gradient approximation (GGA) in the Perdew–Burke–Ernzerhof (PBE) parametrization [34] was applied. For Al and Ni, GGA was shown previously to provide good agreement with experiment for various thermodynamic properties (e.g., Refs. [35,36]). For bulk Ni_3Al, our present calculations show likewise a good agreement between GGA and experiment for different thermodynamic properties (Supplementary Figure S1).

In a periodic supercell approach, the creation of an APB into the supercell is inevitably accompanied by the introduction of periodic image APBs. To efficiently reduce interactions between the APB and its images, we utilized a tilted supercell geometry which was shown to be well-suited for planar defect calculations [37]. In general, the employed supercells consisted of 8 and 9 atomic layers in the direction perpendicular to the (100)APB and the (111)APB, respectively, as displayed in Fig. 1(a) and (b) (except for the magnetic calculations of the (111)APB where 6 layers were used). These separations allow, in particular, the local magnetic moments to approach their bulk values as one moves away from the APB (see Figs. 7(a) and 9(a)).

The most relevant computational details specific to the nonmagnetic and magnetic free energy contributions are provided in the following two subsections. Further numerical details are compiled in the Supplementary Information.

2.2. Nonmagnetic free energy contributions

The DFT calculations for the nonmagnetic contributions were performed using the Vienna Ab initio Simulation Package (VASP) [38,39] with potentials based on the projector augmented wave (PAW) method [40]. For all nonmagnetic calculations, a $2 \times 3 \times 4$ supercell containing 96 atoms was used for the (100)APB and a $2 \times 2 \times 3$ supercell containing 144 atoms for the (111)APB (see Table S1 in the Supplementary Information).

The energy-volume dependence $E_{0K}(V)$ was obtained by fitting the Vinet equation of state [41] to energies for a sufficient number of volumes around the 0 K equilibrium volume. For each volume, the energy was obtained by optimizing atomic positions in all directions for a fixed cell shape, assuming that the APB is surrounded and constrained by the bulk environment. To evaluate a possible influence of anisotropic distortions in the APB, cell shape relaxations were also performed and are discussed in the Supplementary Information.

The electronic free energy F^{el} for the static lattice was computed on a mesh of 4×4 volume and temperature points (see Table S1 in the Supplementary Information) using the finite temperature extension to DFT [42]. The volume and temperature dependencies of the electronic free energy surface were then parametrized as discussed in Ref. [43]. The additional contribution to F^{el} due to thermal vibrations [44], shown to be significant for fcc Ni [37], was included in the vibrational free energy calculations as described below.

The vibrational contribution to the free energy from non-interacting but volume-dependent phonons, F^{qh}, was calculated using the finite-displacement approach as implemented in phonopy [45]. The quasi-harmonic free energy was extracted from a dense set of volumes (8 for the (100)APB and 6 for the (111)APB; Table S1 in the Supplementary Information) and parametrized as a function of volume employing a third-order polynomial.

The anharmonic vibrational free energy F^{ah} resulting from phonon–phonon interactions was computed employing the direct upsampling technique [32] aided by machine-learning interatomic potentials, i.e., moment tensor potentials (MTPs) [46,47], to achieve the required DFT accuracy. Within direct upsampling, the anharmonic free energy is expressed as

$$F^{ah} = \Delta F^{qh\to MTP} + \Delta F^{up}, \quad (5)$$

where the first term $\Delta F^{qh\to MTP}$ is obtained from thermodynamic integration and the second term ΔF^{up} from free energy perturbation theory. Specifically,

$$\Delta F^{qh\to MTP} = \int_0^1 d\lambda \, \langle E^{MTP} - E^{qh} \rangle_\lambda \quad (6)$$

represents a thermodynamic integration with the coupling parameter λ connecting the quasiharmonic reference with energy E^{qh} to the full vibrational energy E^{MTP} described by an MTP. MTPs were shown to accurately describe the full vibrational free energy even of complex systems [48]. With the DFT database for all investigated phases (APB and bulk), we fitted one optimized MTP with a root-mean-square error of below 0.5 meV/atom. The thermodynamic integration was performed for a 4×4 set of volume and temperature points. For each (V,T) point, a dense set of 21 λ values was used to capture the nonlinear dependence of the integrand. For each λ, a molecular dynamics simulation was run until a standard error in the range of 0.1 meV/atom was reached.

The second term in Eq. (5), the so-called upsampling term, accounts for the free energy difference between MTP and DFT in a perturbative manner. Specifically, the full free energy perturbation expression reads

$$\Delta F^{up} = -k_B T \ln \left\langle \exp\left(-\frac{E^{DFT} - E^{MTP}}{k_B T} \right) \right\rangle_{MTP}, \quad (7)$$

where k_B is the Boltzmann constant and E^{DFT} and E^{MTP} are DFT and MTP energies of molecular dynamics snapshots obtained from MTP trajectories. We computed ΔF^{up} for the same (V,T) mesh as the thermodynamic-integration term in Eq. (6). The impact of thermal vibrations on the electronic free energy F^{el} was taken into account by setting the electronic temperature in the DFT calculations to the respective molecular dynamics temperature.

The anharmonic free energies obtained from Eq. (5) for the 4×4 set of (V,T) points were fitted to a smooth anharmonic free energy surface in terms of a renormalized frequency $\bar{\omega}^{ah}(V,T) = a_0 + a_1 V + a_2 T$, where a_0, a_1, and a_2 are fitting coefficients, as detailed in Ref. [35].

In principle, the bulk free energies entering the difference in Eq. (1) to obtain the APB energy are the same for the (100)APB and the (111)APB. Yet, from a numerical perspective, the accuracy of the difference can be improved when the same supercell sizes and orientations are used for the bulk as for the respective APB calculations, in particular for the vibrational free energies. Therefore, the vibrational free energies for the perfect bulk (both quasiharmonic and anharmonic) were computed twice, once in a supercell consistent with the (100)APB supercell geometry and additionally in a supercell consistent with the (111)APB geometry. These calculations yielded very similar results for the vibrational bulk free energies, substantiating that the chosen supercells are well converged.

2.3. Magnetic free energy contribution

For a given (V,T) point, the magnetic free energy in Eq. (3) can be in general expressed as

$$F^{\mathrm{mag}}(V,T) = \min_{\{m_i\}} \left[E^{\mathrm{mag}}(\{m_i\}) - TS^{\mathrm{mag}}(\{m_i\}) \right], \tag{8}$$

where $E^{\mathrm{mag}}(\{m_i\})$ and $S^{\mathrm{mag}}(\{m_i\})$ are, respectively, the magnetic energy and the magnetic entropy for a corresponding magnetic configuration $\{m_i\}$, with m_i denoting the mean local magnetic moment at site i. The minimization to obtain the free energy is performed over different $\{m_i\}$.

In the present work, the magnetic free energy was specifically computed in the single-site mean-field approximation, i.e., magnetic short-range order was neglected, which is a good approximation in Ni_3Al above room temperature. Within this approximation, $E^{\mathrm{mag}}(\{m_i\})$ corresponds to the longitudinal spin fluctuation (LSF) energy computed for a disordered local moment (DLM) spin configuration, and the magnetic entropy, S^{mag}, can be written as [27]

$$S^{\mathrm{mag}}(\{m_i\}) = 3\sum_i \ln(m_i), \tag{9}$$

which corresponds to the classical limit of the LSF entropy, far above the magnetic transition temperature for a quadratic form of $E^{\mathrm{mag}}(\{m_i\})$.

The DLM-LSF energy $E^{\mathrm{mag}}(\{m_i\})$ was computed self-consistently by the exact muffin-tin orbital (EMTO) method [49–52] using the coherent potential approximation (CPA) in the DLM paramagnetic state. In particular, the Lyngby version [53] of the EMTO code was used, which includes an efficient treatment of the magnetic disorder and self-consistent determination of the m_i due to spin fluctuations at the given temperature.

The self-consistent electronic structure calculations were done within the local density approximation using the Perdew and Wang functional [54], while the total energy was calculated using the full charge-density technique [49] in the PBE GGA [34]. Numerical details of the EMTO calculations are given in the Supplementary Information.

The impact of volume and temperature on the set of local magnetic moments $\{m_i\}_{V,T}$ was considered at two levels of approximation. (1) In the first approach, we utilized the thermal expansion from the nonmagnetic calculations and computed the moments for a static lattice at the respective expanded volume. (2) In the second approach, we took molecular dynamics snapshots from the nonmagnetic configurations at two temperatures (600 K and 1000 K) and the respective expanded volumes such as to additionally include the impact of thermal displacements. In both of the approaches, the impact of electronic temperature on the magnetic moments was fully included.

3. Results and discussion

3.1. APB energies at 0 K

Fig. 2 shows the non-relaxed and relaxed (atomic relaxation along all directions while keeping the cell shape and volume fixed) APB energies at 0 K from ferromagnetic (FM) and nonmagnetic (NM) calculations. The reduction of the (100)APB energy due to relaxation is around 15 mJ/m^2. For the (111)APB, a stronger decrease of about 117 mJ/m^2 is observed. For both, relaxed and non-relaxed cases, the spin-polarized ferromagnetic calculations give higher APB energies than the nonmagnetic calculations, cf. the blue bar *versus* the gray bar in each column. For the same type of APB, the increase in APB energy due to spin-polarization is similar, regardless of relaxation.

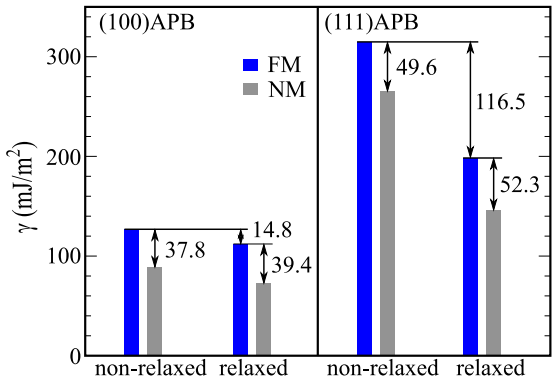

Fig. 2. APB energies under different relaxation and magnetic conditions at 0 K. The energy changes between different calculation conditions are highlighted by vertical arrows with values attached in mJ/m^2. (For interpretation of the references to color in this figure legend, the reader is referred to the web version of this article.)

3.2. Temperature-dependent APB energies

The *ab initio* computed temperature-dependent APB energies, $\gamma_{100}(T)$ and $\gamma_{111}(T)$, are shown in Fig. 3(a) and (b). The solid black lines represent the final prediction with full account of the different thermal excitations that are supposed to guarantee accurate results at elevated temperatures.

Thermal lattice vibrations, including the full impact of explicit anharmonicity, have a moderate temperature-dependent influence on the (100) and (111)APB energies (gray dashed lines labeled "0K + qh + ah"). It is important to stress that fully anharmonic vibrations are required to obtain the observed vibrational dependencies. The quasi-harmonic approximation is not sufficient in this respect. Specifically, at the melting point, the quasiharmonic approximation overestimates both APBs by 30 mJ/m^2 (cf. change from the dotted to the dashed gray lines, indicated by the gray arrows labeled "ah"). This amounts to 30% of the full vibrational value for the (100)APB and 15% for the (111)APB.

Electronic excitations, including the coupling to fully anharmonic atomic vibrations, show a strong and qualitatively similar impact on both APBs. Specifically, the APB energies are increased as temperature increases (change from the gray dashed to the gray dashed–dotted lines indicated by the gray arrows labeled "el"). The maximum impact of electronic excitations is 45 mJ/m^2 (43%) for the (100)APB (at 1400 K) and 39 mJ/m^2 (20%) for the (111)APB (at 1500 K).

Spin fluctuations are – quite unexpectedly for a weak ferromagnetic material – likewise clearly important to obtain accurate APB energies in the paramagnetic state (solid black lines). Qualitatively, we observe a similar impact of spin fluctuations on both APBs (Fig. 3(c) and (d)), i.e., an increase of the APB energies at low and medium temperatures and a decrease at high temperatures. Though qualitatively similar, the quantitative dependencies are different for the (100) and (111)APB. In particular, the spin fluctuation contribution to the (100)APB is significantly stronger. An increase of up to 30 mJ/m^2 can be observed which amounts to nearly 40% of the nonmagnetic data as demonstrated in Fig. 3(c). For the (111)APB, the calculations predict a maximum impact of spin fluctuations of about 15 mJ/m^2, i.e., half of the contribution for the (100)APB. The relative change caused by spin fluctuations amounts to 10% with respect to the nonmagnetic results for the (111)APB.

The temperature dependence of the paramagnetic APB energies reflected by the black solid curves in Fig. 3(a) and (b) corresponds to a parametrization of a dense set of explicit calculations at various temperatures as indicated by the green up-triangles in Fig. 3(c) and (d), respectively. These calculations were done for static lattices including the impact of lattice expansion and electronic excitations.

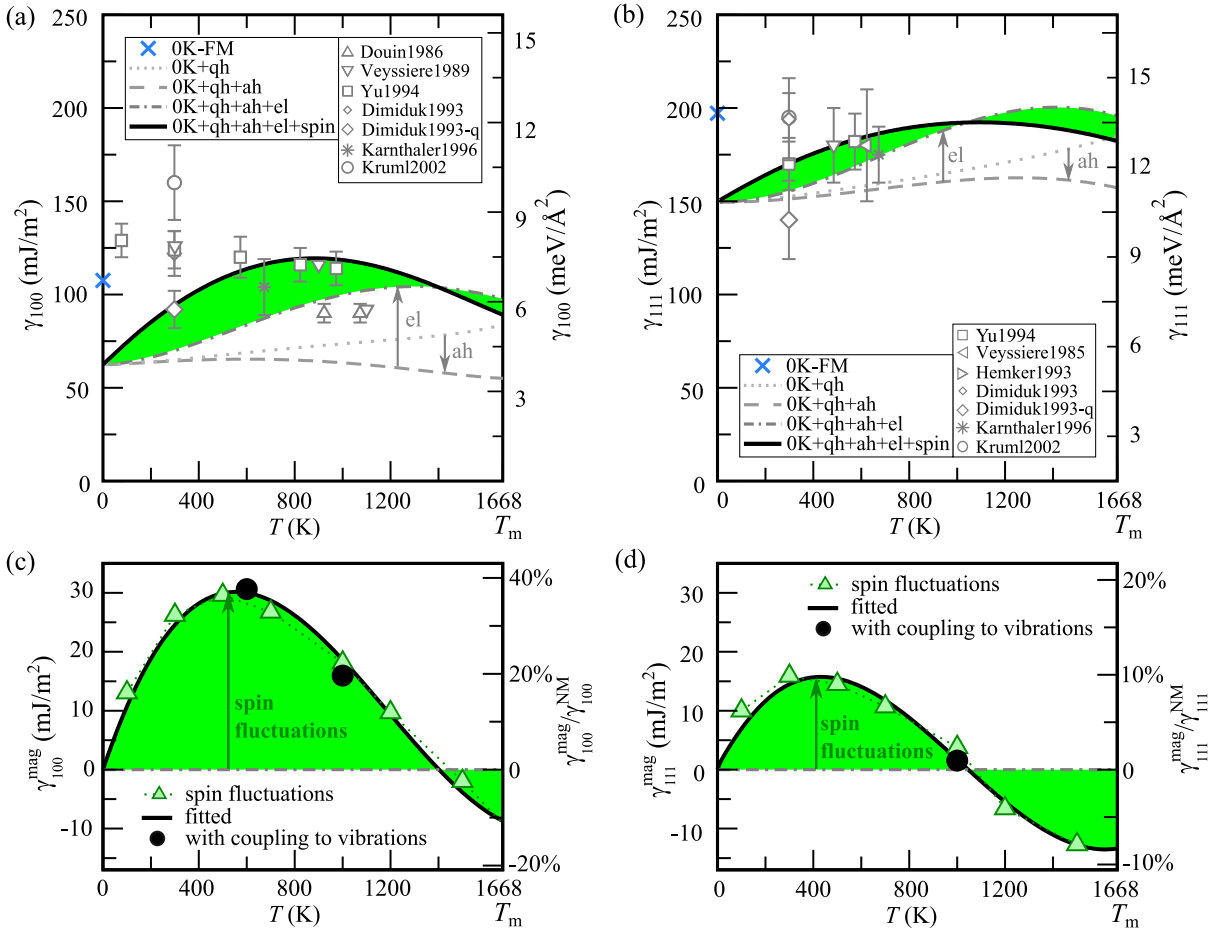

Fig. 3. Formation Gibbs energies for (100) and (111) APBs. (a), (b) Respective temperature-dependent Gibbs energies, γ_{100} and γ_{111}, up to the melting temperature, T_m. The gray dotted lines show the quasiharmonic contribution (qh) and the gray dashed lines represent the full vibrational contribution including explicit anharmonicity (ah). The gray dot-dashed curves contain additionally electronic excitations (el). The solid black curves show the final, paramagnetic results including additionally the impact of spin fluctuations. The contribution of spin fluctuations is highlighted by the green shaded region and emphasized separately in (c) and (d) (γ_{100}^{mag}, γ_{111}^{mag}), in relation to the non-magnetic APB energies (γ_{100}^{NM}, γ_{111}^{NM}; gray dashed lines from (a) and (b)). Up-triangles connected with dotted lines in (c) and (d) represent explicit calculations, used to fit the black curves with third-order polynomials. The filled circles show results of spin fluctuation calculations including the coupling to explicit vibrations. Symbols with error bars in (a) and (b) represent experimental data, i.e., Veyssiere1985 [12] and Veyssiere1989 [14]; Douin1986 [13]; Dimiduk1993 and Dimiduk1993-q [15]; Yu1994 [5]; Karnthaler1996 [7]; Hemker1993 [16]; Kruml2002 [8]. See Supplementary Information for more details on the experimental values.

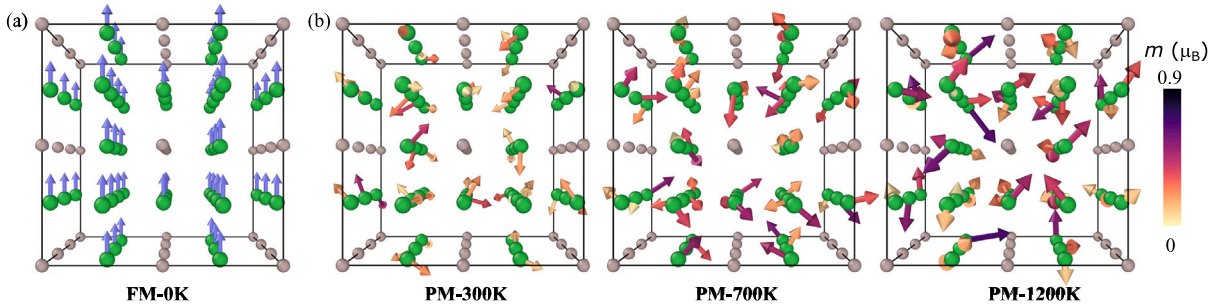

Fig. 4. Schematic of the (a) ferromagnetic (FM) and (b) paramagnetic (PM) state at representative temperatures.

To investigate the explicit impact of lattice vibrations on spin fluctuations, which was shown to be relevant for the thermal conductivity of paramagnetic CrN [28], we selected uncorrelated configurations from molecular dynamics calculations at different representative temperatures, i.e., 600 K and 1000 K for the (100)APB and 1000 K for the (111)APB. The results (filled black circles in Fig. 3(c) and (d)) reveal that the vibrational coupling effect is small for the APB energies of Ni_3Al. The observed magnetic entropy contribution is thus mostly driven by thermally induced spin fluctuations and the lattice expansion, irrespective of explicit thermal lattice vibrations. A similar observation was made for fcc Ni [55], where – despite strong spin fluctuations – the averaged magnetic exchange parameters from molecular dynamics configurations were close to their counterparts from ideal fcc calculations at the expanded lattice constant.

3.3. Magnetic states of bulk Ni_3Al

3.3.1. Ferromagnetic approximation

To reveal the physical origin of the strong impact of spin fluctuations on the APBs, it is insightful to analyze the magnetic moments

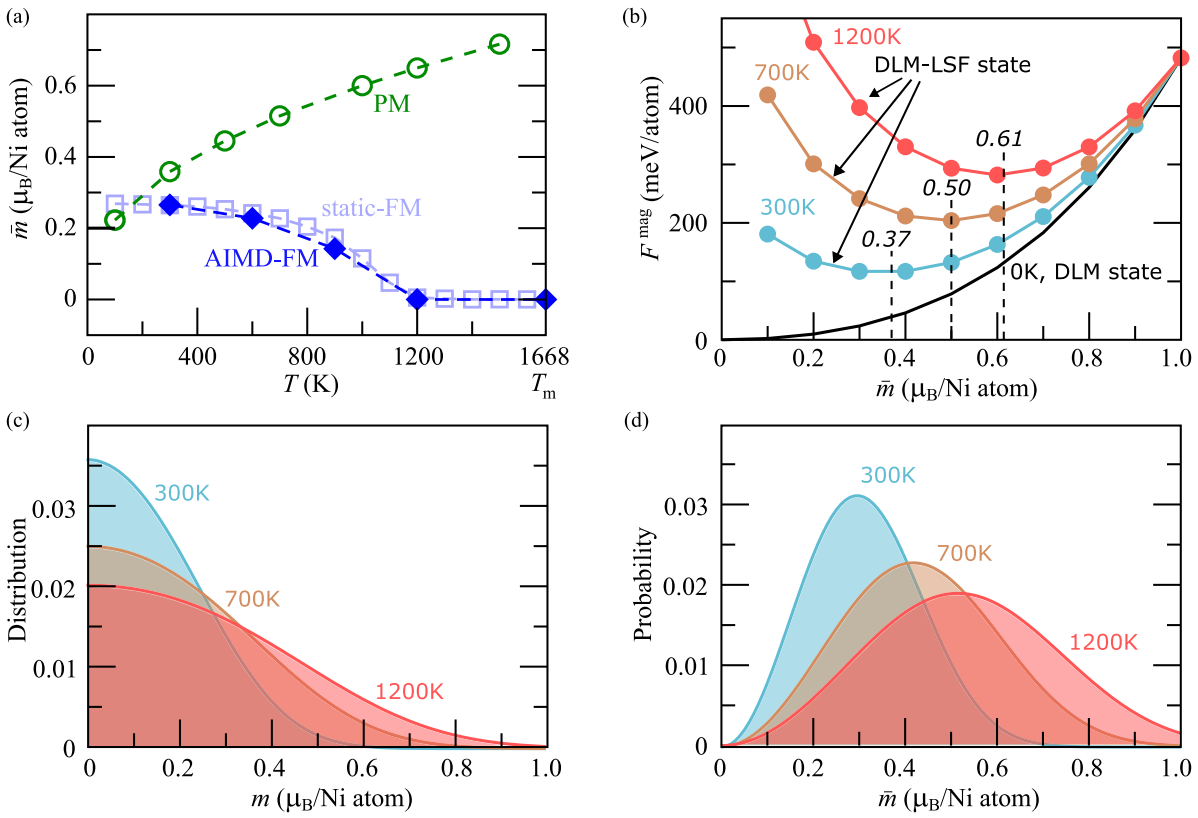

Fig. 5. (a) Mean magnetic moment $\bar{m}$ per Ni atom up to the melting temperature, T_m. Ferromagnetic values for the static lattice (static-FM) and for *ab initio* molecular dynamics (AIMD-FM) are shown. Magnetic moments in the paramagnetic (PM) state are the results of self-consistent DLM-LSF calculations. (b) Magnetic free energy F^{mag} according to Eq. (10) based on the DLM state shown as the black curve, (c) distribution of local moments, and (d) probability of the mean magnetic moment from paramagnetic calculations at the given temperatures. (For interpretation of the references to color in this figure legend, the reader is referred to the web version of this article.)

behavior in bulk Ni_3Al at elevated temperatures, and to compare it with magnetism in fcc Ni. In particular, it is useful to put the paramagnetic behavior in contrast to spin-polarized ferromagnetic results. In the ferromagnetic state, the magnetic moments are aligned in the same spin direction, as depicted in Fig. 4(a). This spin state was previously utilized to derive approximations to the APB energies in Ni_3Al [21]. For fcc Ni, it was indeed shown that the ferromagnetic state describes well the formation energy of stacking faults over the whole temperature range [37]. Fcc Ni has a Curie temperature of 633 K and a moment of about 0.62 μ_B in the ferromagnetic state. Within the reported spin-polarized *ab initio* molecular dynamics simulations, the moment in fcc Ni was shown to remain stable up to its melting temperature of 1728 K with only a small decrease down to about 0.6 μ_B [37].

The situation in bulk Ni_3Al is strikingly different as displayed in Fig. 5(a) by the blue curves. The low temperature magnetic moment is 0.28 μ_B per Ni atom in the ferromagnetic state, about half the value in fcc Ni, and it decreases fully down to zero at about 1200 K (light-blue curve). This decrease is almost completely driven by electronic excitations. The splitting of the electronic density-of-states into a minority and a majority spin channel responsible for the magnetic moment at low temperatures is overcome by the thermal broadening brought about by the Fermi–Dirac function at elevated temperatures, as shown by Fig. 6. The additional broadening by atomic vibrations is small as revealed by explicit *ab initio* molecular dynamics simulations (cf. the dark-blue and light-blue curves in Fig. 5(a)). Thus, APB energies approximated by the ferromagnetic state can be in error at elevated temperatures.

3.3.2. *Paramagnetic state at elevated temperatures*

In contrast to the FM calculations, the here utilized DLM-LSF calculations capture the relevant spin fluctuations in the paramagnetic state

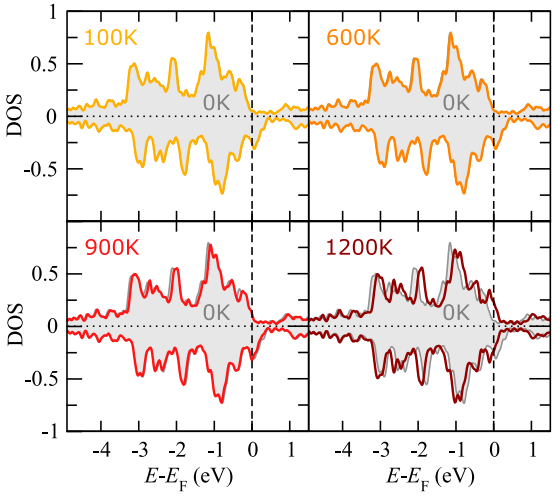

Fig. 6. Electronic DOS' of bulk Ni_3Al at different electronic temperatures for spin-polarized collinear calculations. Positive (negative) DOS' represent the majority (minority) spin channel.

(illustrated in Fig. 4(b)). The resulting mean magnitude of the magnetic moment strongly increases with temperature (green curve in Fig. 5(a)), i.e., from 0.36 μ_B at 300 K to 0.72 μ_B at 1500 K. In Fig. 5(b–d), we demonstrate the mechanism responsible for the strong spin fluctuations in Ni_3Al and explain how it is captured in the DLM-LSF calculations. At zero Kelvin, the DLM (paramagnetic state) energy, $E^{mag}(m)$ has a

minimum at $m = 0$, as shown by the black thick line in Fig. 5(b). At finite temperatures, the magnitude of the Ni local magnetic moment can fluctuate due to thermal excitations, resulting in a distribution function as shown in Fig. 5(c), which is obtained just from standard statistical mechanics [27]. As one can see, the distribution of local magnetic moments is quite broad already at room temperature (blue curve and shading in Fig. 5(c)) and further broadens as temperature increases (700 K and 1200 K are shown as representative temperatures). The probability of finding the specific magnetic moments obtained from these distribution functions is plotted in Fig. 5(d). The magnetic moment corresponding to the maximum probability increases fast with temperature (similar trend as the green curve in Fig. 5(a)).

Eventually, this leads to an additional contribution to the free energy expressed as [27]

$$F^{\mathrm{mag}}(m) = E^{\mathrm{mag}}(m) - TS^{\mathrm{mag}}(m), \tag{10}$$

where $E^{\mathrm{mag}}(m)$ is the magnetic energy obtained from the DLM calculations for the mean magnetic moment m and the magnetic entropy is

$$S^{\mathrm{mag}}(m) = 3\ln(m), \tag{11}$$

which is the exact result if $E^{\mathrm{mag}}(m)$ has a quadratic form as a function of m. The latter is a very good approximation for $E^{\mathrm{mag}}(m)$ in Ni_3Al. The mean magnetic moment m can be found by minimizing the magnetic free energy $F^{\mathrm{mag}}(m)$. Such a minimization is readily performed during the DFT DLM-LSF calculations.

The resulting magnetic free energies are plotted in Fig. 5(b). Free energy curves for three relevant temperatures (300, 700, and 1200 K) are shown. The black curve corresponds to $E^{\mathrm{mag}}(m)$ at 0 K which has a minimum at zero magnetic moment. Hence, without an entropy contribution there is no stable local magnetic moment. As temperature increases, the $-TS^{\mathrm{mag}}$ term becomes more dominant and shifts the minimum in $F^{\mathrm{mag}}(m)$ to higher magnetic moments. The mean magnetic moment minimizing the $F^{\mathrm{mag}}(m)$ curves, $\bar{m}$, (e.g., 0.37 μ_B at 300 K) is close to the result from the self-consistent spin fluctuation calculations (green curve in Fig. 5(a)).

Such entropy-induced magnetic moments on Ni atoms occur also in the vicinity of the APBs. However, there are relevant differences in the stabilization of the moments at the APBs as compared to the perfect bulk, due to the different chemical arrangement of the atoms. These differences drive the observed impact of spin fluctuations on the APB energies (i.e., green shading in Fig. 3), as will be discussed next.

3.4. Interplay between APBs and magnetic moments

The modification of the magnetic moments by the APBs is already apparent for the ferromagnetic state at 0 K, as exemplified in Fig. 7(a) for the (100)APB. The different chemical arrangement of the elements at the APB suppresses locally the magnetic moment down to about 40% (from 0.26 down to 0.1 μ_B). The atomic plane composed of Ni atoms and situated in the center of the (100)APB (layer labeled $l = 0$ in Fig. 7(a)) features a $D0_{22}$ environment for each Ni atom, specifically in the first and second nearest-neighbor shells as clarified in Fig. 7(b). The $D0_{22}$ Ni_3Al crystal structure is nonmagnetic [56], thus explaining the preference of the Ni atoms at the APB to reduce their magnetic moments.

The modification of the magnetic moments is localized to a few layers close to the APB. Already for the $l = 3$ layer, the magnitude of the Ni local magnetic moment is very close to the perfect Ni_3Al bulk value (Fig. 7(a)) and the partial electronic density of states is similar to that in the bulk (Fig. 8). The local chemical environment of Ni at the first and second coordination shells is the same as in the $L1_2$-Ni_3Al structure (Fig. 7(b)). In contrast, the local environment of Ni atoms for $l = 1, 2$, has a mixed character with features from the $L1_2$ and the $D0_{22}$ structure.

At low temperatures, the paramagnetic state shows – similarly to the ferromagnetic state – a reduction of local magnetic moments within a few layers ($l < 3$) of the APB, albeit of a smaller magnitude (Fig. 9(a) and (b)). As temperature increases, the situation changes and the magnetic moments at the APB are enhanced as compared to the bulk. That means that Ni atoms at the APB are more susceptible to spin fluctuations and the entropic stabilization is more effective.

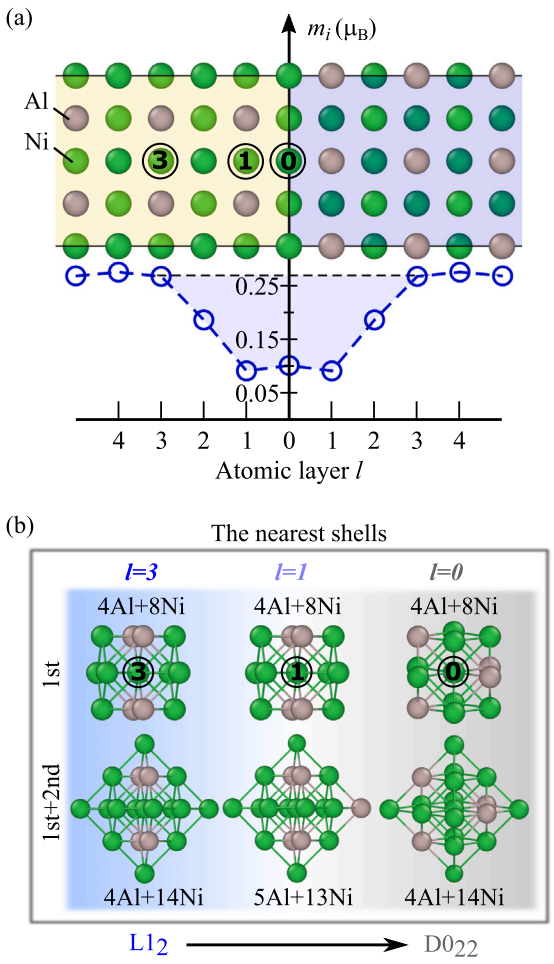

Fig. 7. Impact of the (100)APB on the magnetic moments under the FM condition. (a) Local magnetic moments m_i of Ni atoms as a function of the distance l to the APB plane (in units of (100) atomic layers) in the ferromagnetic state at 0 K. (b) First and second nearest-neighbor environments of three representative Ni atoms as labeled in (a). The change of the chemical arrangement from $L1_2$ to $D0_{22}$ is indicated.

The resulting entropy difference between APB and bulk atoms ($T\Delta s_i$ resolved per lattice site i shown in Fig. 9(c)) shows a similar site and temperature dependence as the local magnetic moment. The maximum contribution from the Ni-site near the APB plane amounts to, for example, 2 meV at 700 K, which is comparable to the ferromagnetic contribution to the APB energy at zero K. The integral of $T\Delta s_i$ over all sites of an APB configuration gives the entropy contribution of spin fluctuations to the APB energy as displayed in Fig. 9(d) (right-triangles). For temperatures below 600 K, the entropy contribution is positive because Δm is negative. At temperatures above 600 K, the entropy contribution is negative and decreases linearly with temperature, because of the positive and increasing Δm. An internal energy contribution (asterisk symbols in Fig. 9(d)) needs to be added to the entropy contribution to arrive at the total contribution of spin fluctuations to the APBs as displayed in Fig. 3(c) and (d).

A similar interplay of the APB with the local magnetic moments as discussed here for the (100)APB is observed for the (111)APB. The respective results are shown in Figure S2 in the Supplementary Information.

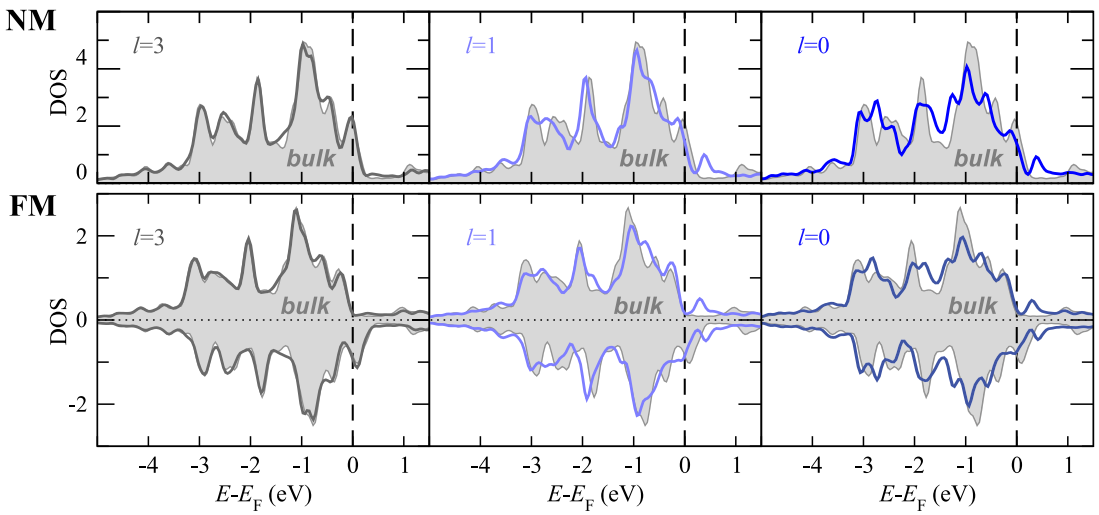

Fig. 8. Partial electronic density of states (DOS) for Ni atoms in the (100)APB structure and bulk Ni_3Al (E_F refers to the Fermi energy). The value of l gives the distance to the APB in terms of atomic layers.

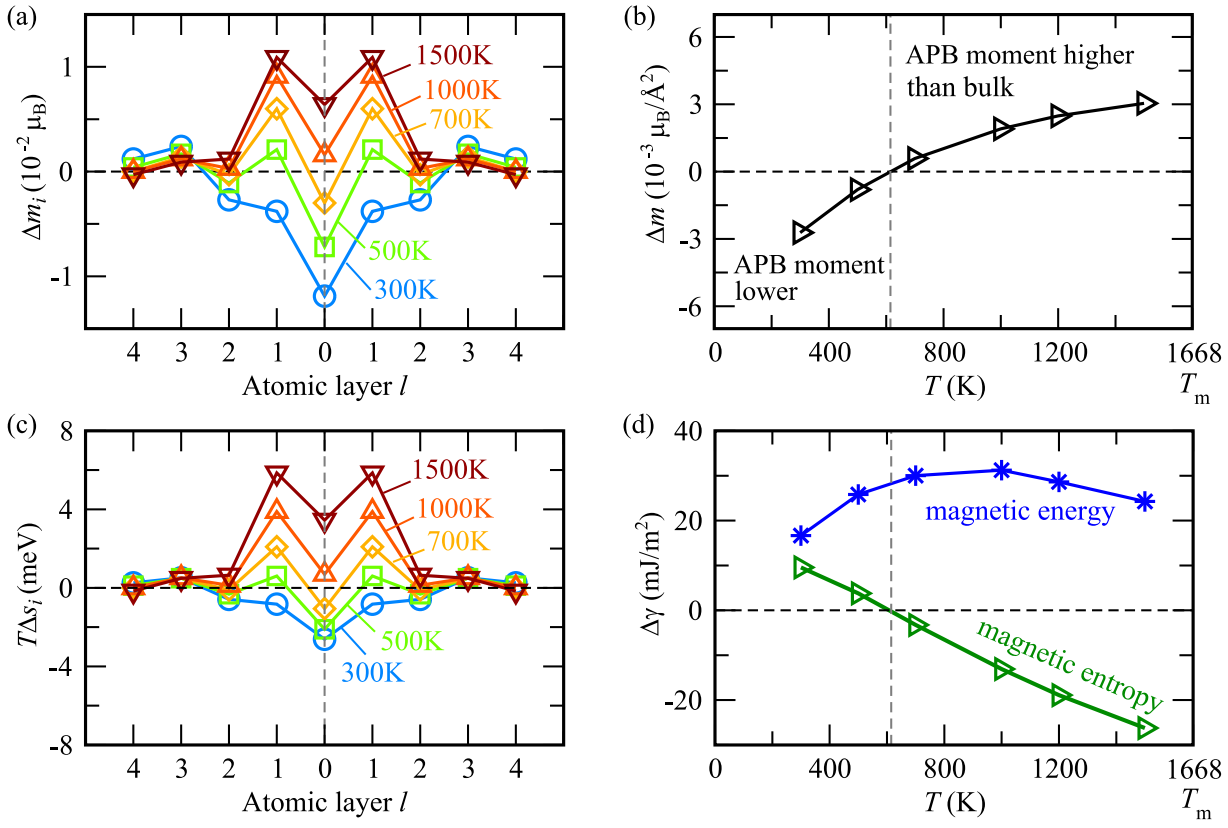

Fig. 9. Impact of the (100)APB on the magnetic moments and the magnetic entropy under the PM condition. (a) Difference in local magnetic moments Δm_i between the (100)APB and perfect bulk in the paramagnetic state at different temperatures. (b) Total difference in the magnetic moments Δm for the (100)APB per unit area. (c) Site-resolved magnetic entropy contribution $T\Delta s_i$ and (d) total magnetic entropy and energy contributions to the (100) APB energy.

3.5. Validity of the calculated APB energies

The utilized approach to capture spin fluctuations is a good approximation well above the Curie temperature T_C, where transverse and longitudinal spin degrees-of-freedom are fully excited. Specifically, our test calculations with the Monte Carlo method indicate that the here predicted spin contribution to the APB energies is accurate at temperatures above ≈300 K. At lower temperatures, in particular in

the vicinity of T_C = 40 K, magnetic short-range-order effects and quantum fluctuations will play an important role and will modify the dependencies [26,57]. Accurate calculations of such effects and their impact on the APB energies close to T_C are presently not possible. At temperatures lower than T_C, one can expect the ferromagnetic 0 K value (light-blue crosses in Fig. 3(a) and (b); zero-point vibrations included) to be a reasonable approximation.

Above 300 K, the paramagnetic prediction of the APB energies (solid black curves in Fig. 3(a) and (b)) can be expected to be reliable. Since explicitly anharmonic atomic vibrations and their coupling to electronic excitations are accounted for, the temperature dependence of the APB energies is in fact accurate up to the melting point. The validity of the prediction is clearly supported by the good agreement of the thermodynamic properties for bulk Ni_3Al with experimental data (see Figure S1 in Supplementary Information). As already emphasized, the inclusion of the different excitation mechanisms, including explicitly anharmonic vibrations, is important to obtain such an accurate prediction at elevated temperatures. It should be particularly stressed that the two APBs, the (100)APB and the (111)APB, are differently affected by the thermal excitations. This is essential, because it is the ratio of the two APB energies that enters the models which describe the YSA in Ni_3Al [9,11].

3.6. Comparison with experimental data

The computed temperature-dependent APB energies can be utilized (above 300 K) to scrutinize the available experimental data. In general, there is good agreement between theory and experiment (Fig. 3). The comparison is facilitated for the (111)APB for which the scatter in experimental results is less than for the (100)APB. At lower temperatures, for the (111)APB, the dissociated dislocations can readily obtain an equilibrium fourfold core structure since the (111) plane is an easy glide plane. The situation is more complicated at higher temperatures, at which the Kear-Wilsdorf lock formation is dominant and (100)APBs prevail in the measurements [5,14,58]. The resulting final paramagnetic curve for the (111)APB energy is in good agreement with the experimental data and can provide a sound prediction in the high temperature range, where experimental measurements are difficult.

For the (100)APB, the simulated APB energy agrees well with a subset of the scattered experimental measurements and thus gives confidence to privilege the respective values. Particularly at low temperatures, experiments may reflect kinetically-trapped, metastable dislocation core structures. For the (100)APB, kinetic traps can easily arise because the (100) plane is energetically unfavorable for dislocation glide at low temperatures [14]. The dislocation dissociation after cross-clip can be therefore significantly suppressed, leading to smaller dissociation distances and consequently higher APB energies. At temperatures at which the Kear-Wilsdorf lock formation sets in, the width of cross-slipped dislocations onto a (100) plane can be as short as 1 nm [59]. Dedicated measurements are necessary to reach equilibrated spacings and thus APB energies.

For an unbiased comparison to experiment, the impact of antisites on the APB energies needs to be considered. Ni on the Al-site was shown to decrease the APB energy whereas Al on the Ni-site acts in the opposite way [60,61]. These theoretical findings are consistent with experimental observations [5,15,62]. Further it is known that the overall density of antisite defects is low at temperatures below 900 K for stoichiometric Ni_3Al [63]. Therefore, in the temperature range most relevant to YSA, antisite defects are likely to play a minor role in Ni_3Al. The here developed methodology could be used in future studies to substantiate this assumption by computing temperature dependent antisite defect Gibbs energies.

4. Summary and outlook

The temperature-dependent (100)APB and (111)APB energies of Ni_3Al have been calculated with *ab initio* accuracy up to the melting temperature. By utilizing the proposed combination of two state-of-the-art methods, all relevant thermal excitations, i.e., thermal magnetic excitations, explicit thermal atomic vibrations, electronic excitations as well as the corresponding coupling effects have been simultaneously taken into account. The resulting temperature-dependent APB energies show a good agreement with the available experimental data.

Electronic excitations significantly increase both APB energies as temperature increases. Atomic vibrations show instead only a moderate influence, which contrasts the behavior found previously for the stacking fault energies of fcc Ni and Al [37].

Quite unexpectedly for a weak ferromagnetic material, we have unveiled – by utilizing DFT-based disordered local moment calculations within the single-site mean-field approximation – that spin fluctuations exhibit a strong impact on APB energies in Ni_3Al. Specifically, we have observed a dramatic increase of the APB energies up to 40% at low and medium temperatures and a decrease at high temperatures.

As revealed in this work, the strong impact of the spin fluctuations on the APB energies originates from an entropy-induced stabilization of the mean magnetic moments. At elevated temperatures, the variations of the magnetic moments due to the change of the local chemical environment in the vicinity of the APB remain significant. This interplay between the APB and the magnetic moments results in an additional contribution to the APB energies.

The presented, *ab initio*-computed temperature-dependent APB energies can be used to explain the experimentally-observed dislocation behavior as well as the YSA phenomenon in Ni_3Al. Specifically, it is believed that the ratio of the APB energies determines the cross-slip tendency [9,10] and thus the probability for Kear-Wilsdorf lock formation. Based on the availability of the APB ratio, quantitative yielding models for Ni-based superalloys become accessible, e.g., in discrete dislocation dynamics or finite element modeling [11]. Thus, an impact on the design and optimization of Ni-based superalloys can be expected. On a broader scale, the obtained comprehensive understanding of APB formation energies could facilitate, for example, defect engineering in other superalloys [64] and in functional materials [65].

The here observed entropy-driven enhancement of the local magnetic moments and their impact on the APB energies demonstrates the necessity to carefully consider paramagnetic effects even for weak itinerant ferromagnetic materials. For an accurate description of high-temperature defect energetics, the inclusion of explicitly anharmonic vibrations, electronic excitations, and coupling effects is likewise required. The proposed combination of state-of-the-art *ab initio* methods can be utilized to properly capture all these effects at reasonable computational expenses.

Declaration of competing interest

The authors declare that they have no known competing financial interests or personal relationships that could have appeared to influence the work reported in this paper.

Data availability

The authors declare that all data supporting the findings are available from the corresponding author upon reasonable request.

Acknowledgments

The authors appreciate the enlightening discussions with Dr. Axel Forslund about the direct upsampling methodology (University of Stuttgart, Germany). This work has been funded by the Deutsche Forschungsgemeinschaft (DFG, German Research Foundation) under the Germany's Excellence Strategy - EXC 2075 – 390740016. We acknowledge the support by the Stuttgart Center for Simulation Science (SimTech). We acknowledge the support by the state of Baden-Württemberg through bwHPC and the German Research Foundation (DFG) through grant no INST 40/575-1 FUGG (JUSTUS 2 cluster) and the support of the Gauss Centre for Supercomputing e.V. for providing computing time on the GCS Supercomputer (HAWK) at the Höchstleistungsrechenzentrum Stuttgart. B.G. acknowledges funding from the European Research Council (ERC) under the European Union's Horizon 2020 research and innovation programme (Grant Agreement No. 865855). A.R. acknowledges the support by the Austrian Federal Government (in particular from Bundesministerium für Verkehr, Innovation und Technologie and Bundesministerium für Wirtschaft, Familie und Jugend) represented by Österreichische Forschungsförderungsgesellschaft mbH and the Styrian and the Tyrolean Provincial Government, represented by Österreichische Forschungsförderungsgesellschaft mbH and Standortagentur Tirol within the framework of the COMET Funding Programme. Calculations have been partly done using NSC (Linköping) and PDC (Stockholm) resources provided by the Swedish National Infrastructure for Computing (SNIC).

Appendix A. Supplementary data

Supplementary material related to this article can be found online at https://doi.org/10.1016/j.actamat.2023.118986.

References

[1] D. Furrer, H. Fecht, Ni-based superalloys for turbine discs, JOM 51 (1) (1999) 14–17, http://dx.doi.org/10.1007/s11837-999-0005-y.

[2] Y.M. Wang-Koh, Understanding the yield behaviour of $L1_2$-ordered alloys, Mater. Sci. Technol. 33 (8) (2017) 934–943, http://dx.doi.org/10.1080/02670836.2016.1215961.

[3] A.J. Goodfellow, Strengthening mechanisms in polycrystalline nickel-based superalloys, Mater. Sci. Technol. 34 (15) (2018) 1793–1808, http://dx.doi.org/10.1080/02670836.2018.1461594.

[4] N. Masahashi, T. Takasugi, O. Izumi, Mechanical properties of Ni_3Al containing C, B and Be, Acta Metall. 36 (7) (1988) 1823–1836, http://dx.doi.org/10.1016/0001-6160(88)90251-9.

[5] H.F. Yu, I.P. Jones, R.E. Smallman, The effects of temperature, composition and strain rate on the deformation microstructure of Ni_3Al, Phil. Mag. A 70 (6) (1994) 951–967, http://dx.doi.org/10.1080/01418619408242942.

[6] B.H. Kear, Dislocation configurations and work hardening in Cu_3Au crystals, Acta Metall. 12 (5) (1964) 555–569, http://dx.doi.org/10.1016/0001-6160(64)90028-8.

[7] H.P. Karnthaler, E.T. Mühlbacher, C. Rentenberger, The influence of the fault energies on the anomalous mechanical behaviour of Ni_3Al alloys, Acta Mater. 44 (2) (1996) 547–560, http://dx.doi.org/10.1016/1359-6454(95)00191-3.

[8] T. Kruml, E. Conforto, B.L. Piccolo, D. Caillard, J.L. Martin, From dislocation cores to strength and work-hardening: a study of binary Ni_3Al, Acta Mater. 50 (20) (2002) 5091–5101, http://dx.doi.org/10.1016/S1359-6454(02)00364-6.

[9] V. Paidar, D.P. Pope, V. Vitek, A theory of the anomalous yield behavior in $L1_2$ ordered alloys, Acta Metall. 32 (3) (1984) 435–448, http://dx.doi.org/10.1016/0001-6160(84)90117-2.

[10] P.B. Hirsch, A model of the anomalous yield stress for (111) slip in $L1_2$ alloys, Prog. Mater. Sci. 36 (1992) 63–88, http://dx.doi.org/10.1016/0079-6425(92)90005-R.

[11] Y.S. Choi, D.M. Dimiduk, M.D. Uchic, T.A. Parthasarathy, Modelling plasticity of Ni_3Al-based $L1_2$ intermetallic single crystals. I. Anomalous temperature dependence of the flow behaviour, Phil. Mag. 87 (12) (2007) 1939–1965, http://dx.doi.org/10.1080/14786430601169782.

[12] P. Veyssière, J. Douin, P. Beauchamp, On the presence of super lattice intrinsic stacking faults in plastically deformed Ni_3Al, Phil. Mag. A 51 (3) (1985) 469–483, http://dx.doi.org/10.1080/01418618508237567.

[13] J. Douin, P. Veyssière, P. Beauchamp, Dislocation line stability in Ni_3Al, Phil. Mag. A 54 (3) (1986) 375–393, http://dx.doi.org/10.1080/01418618608240722.

[14] P. Veyssière, M.H. Yoo, J.A. Horton, C.T. Liu, Temperature effect on superdislocation dissociation on a cube plane in Ni_3Al, Phil. Mag. Lett. 59 (2) (1989) 61–68, http://dx.doi.org/10.1080/09500839008214778.

[15] D.M. Dimiduk, A.W. Thompson, J.C. Williams, The compositional dependence of antiphase-boundary energies and the mechanism of anomalous flow in Ni_3Al alloys, Phil. Mag. A 67 (3) (1993) 675–698, http://dx.doi.org/10.1080/01418619308207184.

[16] K.J. Hemker, M.J. Mills, Measurements of antiphase boundary and complex stacking fault energies in binary and B-doped Ni_3Al using TEM, Phil. Mag. A 68 (2) (1993) 305–324, http://dx.doi.org/10.1080/01418619308221207.

[17] M.H. Yoo, Stability of superdislocations and shear faults in $L1_2$ ordered alloys, Acta Metall. 35 (7) (1987) 1559–1569, http://dx.doi.org/10.1016/0001-6160(87)90102-7.

[18] A.T. Paxton, Y.Q. Sun, The role of planar fault energy in the yield anomaly in $L1_2$ intermetallics, Phil. Mag. A 78 (1) (1998) 85–104, http://dx.doi.org/10.1080/014186198253697.

[19] M. Chandran, S.K. Sondhi, First-principle calculation of APB energy in Ni-based binary and ternary alloys, Modelling Simul. Mater. Sci. Eng. 19 (2) (2011) 025008, http://dx.doi.org/10.1088/0965-0393/19/2/025008.

[20] D.J. Crudden, A. Mottura, N. Warnken, B. Raeisinia, R.C. Reed, Modelling of the influence of alloy composition on flow stress in high-strength nickel-based superalloys, Acta Mater. 75 (2014) 356–370, http://dx.doi.org/10.1016/j.actamat.2014.04.075.

[21] V.R. Manga, S.-L. Shang, W.Y. Wang, Y. Wang, J. Liang, V.H. Crespi, Z.-K. Liu, Anomalous phonon stiffening associated with the (111) antiphase boundary in $L1_2$ Ni_3Al, Acta Mater. 82 (2015) 287–294, http://dx.doi.org/10.1016/j.actamat.2014.09.005.

[22] S. Celotto, W. Eerenstein, T. Hibma, Characterization of anti-phase boundaries in epitaxial magnetite films, Eur. Phys. J. B 36 (2) (2003) 271–279, http://dx.doi.org/10.1140/epjb/e2003-00344-7.

[23] F.R. De Boer, C.J. Schinkel, J. Biesterbos, S. Proost, Exchange-enhanced paramagnetism and weak ferromagnetism in the Ni_3Al and Ni_3Ga phases; giant moment inducement in Fe-doped Ni_3Ga, J. Appl. Phys. 40 (3) (1969) 1049–1055, http://dx.doi.org/10.1063/1.1657528.

[24] T. Moriya, Spin Fluctuations in Itinerant Electron Magnetism, in: Springer Series in Solid-State Sciences, vol. 56, 1985.

[25] A. Georges, G. Kotliar, W. Krauth, M.J. Rozenberg, Dynamical mean-field theory of strongly correlated fermion systems and the limit of infinite dimensions, Rev. Modern Phys. 68 (1996) 13–125, http://dx.doi.org/10.1103/RevModPhys.68.13.

[26] A.V. Ruban, S. Khmelevskyi, P. Mohn, B. Johansson, Temperature-induced longitudinal spin fluctuations in Fe and Ni, Phys. Rev. B 75 (5) (2007) 054402, http://dx.doi.org/10.1103/PhysRevB.75.054402.

[27] A.V. Ruban, A.B. Belonoshko, N.V. Skorodumova, Impact of magnetism on Fe under Earth's core conditions, Phys. Rev. B 87 (1) (2013) 014405, http://dx.doi.org/10.1103/PhysRevB.87.014405.

[28] I. Stockem, A. Bergman, A. Glensk, T. Hickel, F. Körmann, B. Grabowski, J. Neugebauer, B. Alling, Anomalous phonon lifetime shortening in paramagnetic CrN caused by spin-lattice coupling: A combined spin and *Ab Initio* molecular dynamics study, Phys. Rev. Lett. 121 (2018) 125902, http://dx.doi.org/10.1103/PhysRevLett.121.125902.

[29] A. Forslund, X. Zhang, B. Grabowski, A.V. Shapeev, A.V. Ruban, Ab initio simulations of the surface free energy of TiN(001), Phys. Rev. B 103 (2021) 195428, http://dx.doi.org/10.1103/PhysRevB.103.195428.

[30] A. Glensk, B. Grabowski, T. Hickel, J. Neugebauer, Breakdown of the Arrhenius law in describing vacancy formation energies: The importance of local anharmonicity revealed by ab initio thermodynamics, Phys. Rev. X 4 (2014) 011018, http://dx.doi.org/10.1103/PhysRevX.4.011018.

[31] X. Zhang, B. Grabowski, T. Hickel, J. Neugebauer, Calculating free energies of point defects from *ab initio*, Comput. Mater. Sci. 148 (2018) 249–259, http://dx.doi.org/10.1016/j.commatsci.2018.02.042.

[32] Y. Zhou, P. Srinivasan, F. Körmann, B. Grabowski, R. Smith, P. Goddard, A.I. Duff, Thermodynamics up to the melting point in a TaVCrW high entropy alloy: Systematic *ab initio* study aided by machine learning potentials, Phys. Rev. B 105 (21) (2022) 214302, http://dx.doi.org/10.1103/PhysRevB.105.214302.

[33] G.K. Dey, Physical metallurgy of nickel aluminides, Sadhana 28 (1) (2003) 247–262, http://dx.doi.org/10.1007/BF02717135.

[34] J.P. Perdew, K. Burke, M. Ernzerhof, Generalized gradient approximation made simple, Phys. Rev. Lett. 77 (1996) 3865–3868, http://dx.doi.org/10.1103/PhysRevLett.77.3865.

[35] B. Grabowski, L. Ismer, T. Hickel, J. Neugebauer, *Ab initio* up to the melting point: Anharmonicity and vacancies in aluminum, Phys. Rev. B 79 (13) (2009) 134106, http://dx.doi.org/10.1103/PhysRevB.79.134106.

[36] Y. Gong, B. Grabowski, A. Glensk, F. Körmann, J. Neugebauer, R.C. Reed, Temperature dependence of the Gibbs energy of vacancy formation of fcc Ni, Phys. Rev. B 97 (21) (2018) 214106, http://dx.doi.org/10.1103/PhysRevB.97.214106.

[37] X. Zhang, B. Grabowski, F. Körmann, A.V. Ruban, Y. Gong, R.C. Reed, T. Hickel, J. Neugebauer, Temperature dependence of the stacking-fault Gibbs energy for Al, Cu, and Ni, Phys. Rev. B 98 (22) (2018) 224106, http://dx.doi.org/10.1103/PhysRevB.98.224106.

[38] G. Kresse, J. Hafner, Ab initio molecular dynamics for liquid metals, Phys. Rev. B 47 (1993) 558–561, http://dx.doi.org/10.1103/PhysRevB.47.558.

[39] G. Kresse, J. Hafner, Ab initio molecular-dynamics simulation of the liquid-metal–amorphous-semiconductor transition in germanium, Phys. Rev. B 49 (1994) 14251–14269, http://dx.doi.org/10.1103/PhysRevB.49.14251.

[40] G. Kresse, D. Joubert, From ultrasoft pseudopotentials to the projector augmented-wave method, Phys. Rev. B 59 (1999) 1758–1775, http://dx.doi.org/10.1103/PhysRevB.59.1758.

[41] P. Vinet, J. Ferrante, J.H. Rose, J.R. Smith, Compressibility of solids, J. Geophys. Res.: Solid Earth 92 (B9) (1987) 9319–9325, http://dx.doi.org/10.1029/JB092iB09p09319.

[42] N.D. Mermin, Thermal properties of the inhomogeneous electron gas, Phys. Rev. 137 (5A) (1965) A1441, http://dx.doi.org/10.1103/PhysRev.137.A1441.

[43] B. Grabowski, P. Söderlind, T. Hickel, J. Neugebauer, Temperature-driven phase transitions from first principles including all relevant excitations: The fcc-to-bcc transition in Ca, Phys. Rev. B 84 (21) (2011) 214107, http://dx.doi.org/10.1103/PhysRevB.84.214107.

[44] X. Zhang, B. Grabowski, F. Körmann, C. Freysoldt, J. Neugebauer, Accurate electronic free energies of the 3*d*, 4*d*, and 5*d* transition metals at high temperatures, Phys. Rev. B 95 (16) (2017) 165126, http://dx.doi.org/10.1103/PhysRevB.95.165126.

[45] A. Togo, I. Tanaka, First principles phonon calculations in materials science, Scr. Mater. 108 (2015) 1–5, http://dx.doi.org/10.1016/j.scriptamat.2015.07.021.

[46] A.V. Shapeev, Moment tensor potentials: A class of systematically improvable interatomic potentials, Multiscale Model. Simul. 14 (3) (2016) 1153–1173, http://dx.doi.org/10.1137/15M1054183.

[47] K. Gubaev, E.V. Podryabinkin, G.L.W. Hart, A.V. Shapeev, Accelerating high-throughput searches for new alloys with active learning of interatomic potentials, Comput. Mater. Sci. 156 (2019) 148–156, http://dx.doi.org/10.1016/j.commatsci.2018.09.031.

[48] B. Grabowski, Y. Ikeda, P. Srinivasan, F. Körmann, C. Freysoldt, A.I. Duff, A. Shapeev, J. Neugebauer, Ab initio vibrational free energies including anharmonicity for multicomponent alloys, Npj Comput. Mater. 5 (1) (2019) 1–6, http://dx.doi.org/10.1038/s41524-019-0218-8.

[49] L. Vitos, Computational Quantum Mechanics for Materials Engineers: The EMTO Method and Applications, Springer Science & Business Media, 2007.

[50] L. Vitos, H.L. Skriver, B. Johansson, J. Kollár, Application of the exact muffin-tin orbitals theory: the spherical cell approximation, Comput. Mater. Sci. 18 (1) (2000) 24–38, http://dx.doi.org/10.1016/S0927-0256(99)00098-1.

[51] L. Vitos, Total-energy method based on the exact muffin-tin orbitals theory, Phys. Rev. B 64 (1) (2001) 014107, http://dx.doi.org/10.1103/PhysRevB.64.014107.

[52] L. Vitos, I.A. Abrikosov, B. Johansson, Anisotropic lattice distortions in random alloys from first-principles theory, Phys. Rev. Lett. 87 (15) (2001) 156401, http://dx.doi.org/10.1103/PhysRevLett.87.156401.

[53] A.V. Ruban, M. Dehghani, Atomic configuration and properties of austenitic steels at finite temperature: Effect of longitudinal spin fluctuations, Phys. Rev. B 94 (2016) 104111, http://dx.doi.org/10.1103/PhysRevB.94.104111.

[54] J.P. Perdew, Y. Wang, Accurate and simple analytic representation of the electron-gas correlation energy, Phys. Rev. B 45 (1992) 13244–13249, http://dx.doi.org/10.1103/PhysRevB.45.13244.

[55] A.V. Ruban, O.E. Peil, Impact of thermal atomic displacements on the Curie temperature of 3d transition metals, Phys. Rev. B 97 (17) (2018) 174426, http://dx.doi.org/10.1103/PhysRevB.97.174426.

[56] J.H. Xu, B.I. Min, A.J. Freeman, T. Oguchi, Phase stability and magnetism of Ni_3Al, Phys. Rev. B 41 (8) (1990) 5010, http://dx.doi.org/10.1103/PhysRevB.41.5010.

[57] F. Körmann, T. Hickel, J. Neugebauer, Influence of magnetic excitations on the phase stability of metals and steels, Curr. Opin. Solid State Mater. Sci. 20 (2) (2016) 77–84, http://dx.doi.org/10.1016/j.cossms.2015.06.001.

[58] N. Baluc, R. Schäublin, Weak beam transmission electron microscopy imaging of superdislocations in ordered Ni_3Al, Phil. Mag. A 74 (1) (1996) 113–136, http://dx.doi.org/10.1080/01418619608239693.

[59] G. Molénat, D. Caillard, Investigations of dislocation mechanisms in Ni_3Al at different temperatures: *in situ* straining experiments in a transmission electron microscope, Phil. Mag. A 69 (5) (1994) 939–959, http://dx.doi.org/10.1080/01418619408242529.

[60] P. Hu, W. Zhao, Y. Ru, Y. Pei, S. Li, H. Xu, Effects of intrinsic point defects on antiphase boundary energy of γ'-Ni_3Al from first-principles calculations, J. Mater. Sci. 57 (27) (2022) 12916–12928, http://dx.doi.org/10.1007/s10853-022-07445-9.

[61] K. Kumar, R. Sankarasubramanian, U.V. Waghmare, Tuning planar fault energies of Ni_3Al with substitutional alloying: First-principles description for guiding rational alloy design, Scr. Mater. 142 (2018) 74–78, http://dx.doi.org/10.1016/j.scriptamat.2017.08.021.

[62] O.I. Gorbatov, I.L. Lomaev, Y.N. Gornostyrev, A.V. Ruban, D. Furrer, V. Venkatesh, D.L. Novikov, S.F. Burlatsky, Effect of composition on antiphase boundary energy in Ni_3Al based alloys: Ab initio calculations, Phys. Rev. B 93 (2016) 224106, http://dx.doi.org/10.1103/PhysRevB.93.224106.

[63] C. Harris, R. Tedstrom, M.S. Daw, M.J. Mills, Calculations of diffusion and diffusion-limited processes in Ni_3Al using accelerated molecular dynamics, Comput. Mater. Sci. 37 (4) (2006) 462–469, http://dx.doi.org/10.1016/j.commatsci.2005.11.005.

[64] A. Suzuki, H. Inui, T.M. Pollock, $L1_2$-strengthened cobalt-base superalloys, Annu. Rev. Mater. Res. 45 (2015) 345–368, http://dx.doi.org/10.1146/annurev-matsci-070214-021043.

[65] Z. Wang, H. Guo, S. Shao, M. Saghayezhian, J. Li, R. Fittipaldi, A. Vecchione, P. Siwakoti, Y. Zhu, J. Zhang, et al., Designing antiphase boundaries by atomic control of heterointerfaces, Proc. Natl. Acad. Sci. 115 (38) (2018) 9485–9490, http://dx.doi.org/10.1073/pnas.1808812115.